Chemical Engineering Journal 512 (2025) 162687

Contents lists available at ScienceDirect

Chemical Engineering Journal

journal homepage: www.elsevier.com/locate/cej

CeO_2 and Nb_2CT_x heterojunction for efficient room-temperature NH_3 detection

Dingyuan Wang [a], Lizhai Zhang [a,b,c,*], Jiayuan Xu [d], Xinyu Lei [a], Henghui Sun [a], Fei Ma [b], Taotao Ai [a,*], Paul K. Chu [c,*]

[a] School of Materials Science and Engineering, Shaanxi University of Technology, Hanzhong 723001 Shaanxi, China
[b] State Key Laboratory for Mechanical Behavior of Materials, Xi'an Jiaotong University, Xi'an 710049 Shaanxi, China
[c] Department of Physics, Department of Materials Science and Engineering, and Department of Biomedical Engineering, City University of Hong Kong, Tat Chee Avenue, Kowloon, Hong Kong, China
[d] Natural Active Industrialization Engineering Technology Research Centre of Shaanxi Province, Shaanxi University of Technology, Hanzhong 723001 Shaanxi, China

ARTICLE INFO

Keywords:
Heterojunction
CeO_2/Nb_2CT_x composite
NH_3 sensing
First-principles calculation

ABSTRACT

Although metal oxides are attractive to gas sensing, the low response, high working temperature, and poor selectivity hamper widespread applications. Herein, a room-temperature NH_3 gas sensor constructed with CeO_2 nanoparticles functionalized Nb_2CT_x MXene is designed and demonstrated. Compared to CeO_2, the response to NH_3 increases by 4 times. The other merits include a low detection limit, excellent repeatability, long-term stability, as well as rapid response and recovery. The enhanced NH_3 sensing performance can be attributed to several factors. Firstly, the unique layered structure of CeO_2/Nb_2CT_x composites increases the surface area to improve the adsorption and diffusion ability of NH_3. Secondly, introduction of Nb_2CT_x could promote formation of oxygen vacancy in CeO_2, increasing the density of active sites and promoting adsorption of NH_3. Thirdly, a heterojunction is formed at interface to boost electron transfer and the sensing capability. The results reveal a novel strategy to develop metal oxide and MXene heterojunctions for sensitive and reliable detection of NH_3.

1. Introduction

Ammonia is a common toxic gas, which poses certain hazards to human health [1,2]. Inhaling high concentrations of NH_3 causes respiratory irritation, leading to coughing, difficulty breathing, and throat discomfort [3–5]. Even at low concentrations, the pungent odor of NH_3 can cause headaches, nausea, and fatigue [6]. In addition, the release of NH_3 into the environment may cause pollution to water and soil and affect the balance of ecosystem [7]. Hence, it is essential to develop a highly responsive, selective, and stable sensor to detect NH_3 accurately for environmental monitoring.

Because of the abundant resources, low production cost, and flexible preparation, metal oxide semiconductors have a large potential in NH_3 sensing [8–10]. NH_3 sensors consisting of different metal oxides have been reported, for instance, SnO_2 [11,12], WO_3 [13,14], CeO_2 [6,15,16], ZnO [17], Cr doped ZnO [18], and so on. Among them, CeO_2 is especially attractive on account of oxygen vacancy defects, high earth abundance, and robust chemical and structural stability. However, CeO_2-based gas sensors are sensitive to not only NH_3 but also NO_2, and the selectivity tends to be poor. The high operating temperature requires large energy consumption and causes safety issues and poor stability. In addition, the stacking of the CeO_2 nanoparticles obstructs the diffusion of gas molecules, causing insufficient utilization of active surface sites. Therefore, it is challenging to design a room-temperature CeO_2-based NH_3 sensor with high response, high selectivity, low detection limit, and good reversibility.

To address these challenges, composites have been developed. For instance, ***Sinha et al.*** successfully synthesized NiO and CeO_2 composites by electrospinning with good NH_3 sensing properties at room temperature (RT). Compared to pure NiO, the RT response to 10 ppm NH_3 is enhanced by 106 %, in addition to the superior selectivity, stability, and response time [19]. ***Wang et al.*** synthesized composites of CeO_2 and PANI by *in situ* polymerization. At RT, although CeO_2 exhibits no response to NH_3, the introduction of PANI increases the response to 84.61 %, and the detection time is only 57.6 s [20]. These results reveal the structural advantages of multi-component materials with less self-stacking of nanoparticles. Meanwhile, the heterojunction formed at interface can improve charge transfer and gas-sensing response. Nb_2CT_x,

* Corresponding authors at: School of Materials Science and Engineering, Shaanxi University of Technology, Hanzhong 723001, Shaanxi, China.
E-mail addresses: zhanglizhai0512@snut.edu.cn (L. Zhang), aitaotao0116@126.com (T. Ai), paul.chu@cityu.edu.hk (P.K. Chu).

https://doi.org/10.1016/j.cej.2025.162687
Received 26 November 2024; Received in revised form 2 March 2025; Accepted 15 April 2025
Available online 15 April 2025
1385-8947/

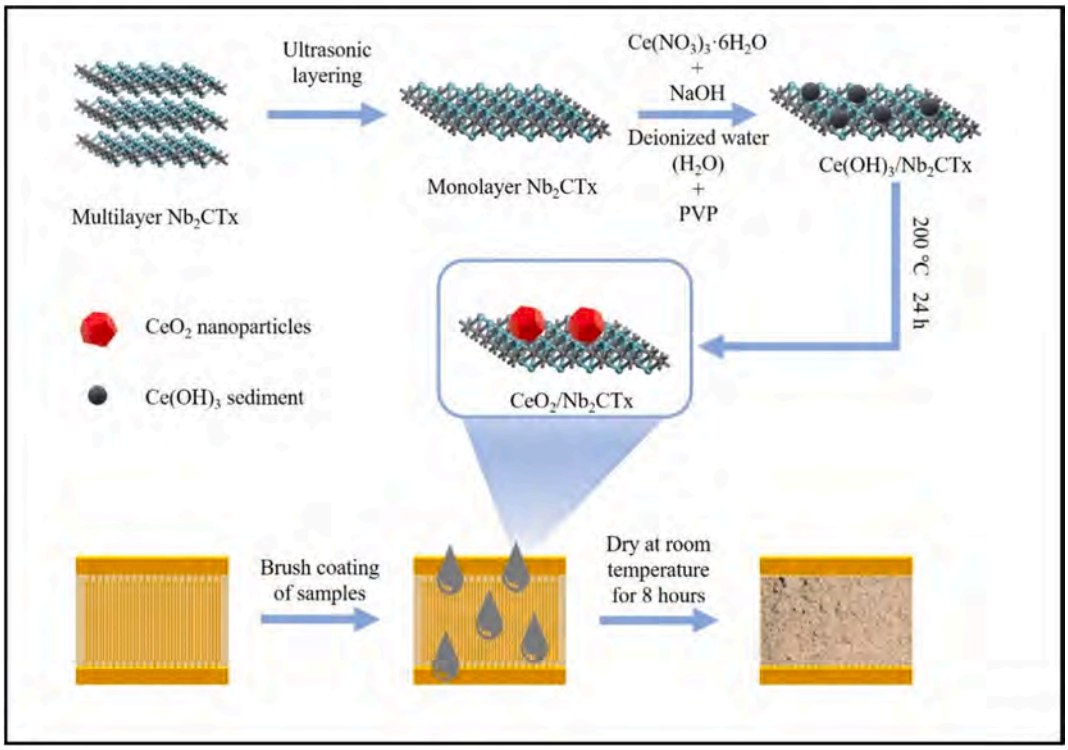

Fig. 1. Preparation of CeO_2/Nb_2CT_x composites and sensors.

as the new class of 2D MXene materials, consists of accordion-like delaminated layers with a large surface area and excellent electrical conductivity. The surface terminal groups and defects in Nb_2CT_x provide the active sites to adsorb NH_3 molecules. Therefore, if the CeO_2 nanoparticles are deposited on Nb_2CT_x, the room-temperature NH_3-sensing response may be enhanced.

Herein, the compounds of CeO_2 and Nb_2CT_x are prepared hydrothermally. Nb_2CT_x with a large surface serves as a template for the growth of CeO_2 nanoparticles to prevent restacking of CeO_2 and oxidation of Nb_2CT_x, resulting in more sites for NH_3 adsorption. Compared to pure CeO_2, the room-temperature response of composite improves by 4 times, in addition to the excellent selectivity, long-term stability, and shorter response and recovery time. First-principles calculations are performed to elucidate the enhancement mechanism.

2. Experimental details

2.1. Construction of CeO_2/Nb_2CT_x heterostructure

The CeO_2/Nb_2CT_x compounds was prepared by a hydrothermal method. As illustrated in Fig. 1, the hydrofluoric acid is used as an etchant to prepare Nb_2CT_x. In brief, Nb_2CT_x was dispersed in 30 mL of deionized water (DI) and then sonicated for 30 min. 200 mg of $Ce(NO_3)_3{\cdot}6H_2O$, 80 mg of NaOH, and 300 mg of polyvinyl pyrrolidone (PVP) were added to the solution and stirred for 90 min. The mixture was transferred into a Telfon-lined autoclave (50 mL) and heated to 200 ℃ for 24 h. The precipitate was then centrifuged, washed three times with deionized water and alcohol, and dried for 10 h in a vacuum oven at 60 ℃. To study the effects of the amount of Nb_2CT_x, samples with 0.25 wt% (0.5 mg), 0.5 wt% (1 mg), 1.5 wt% (3 mg), and 2.5 wt% (5 mg) Nb_2CT_x were synthesized and then marked as C/N-a, C/N-b, C/N-c, and C/N-d, respectively.

2.2. Materials characterization

The crystal structure and phase were characterized by X-ray diffraction (XRD, D/max-2200PC) with Cu K_α radiation. Raman scattering measurements were performed using the Horiba LabRAM HR Evolution spectrometer, equipped with a 514 nm laser and operated at 2 mW power. The integration time was set as 50 s, and the grating resolution was 2400 gr/mm. Scanning electron microscopy (SEM, JSM-7610F) and transmission electron microscopy (TEM, JEM-2100P) were used to examine the microstructure and morphology of samples. X-ray photoelectron spectroscopy (XPS, Thermo Scientific K-Alpha) was conducted to determine the chemical states. Electron paramagnetic resonance (EPR) was carried out on the A300 Bruker EPR with an X-band frequency of 9.4 GHz, 100 kHz field modulation frequency, and 1.0 G standard modulation amplitude. The work function was determined by ultraviolet photoelectron spectroscopy (UPS, Thermo Fisher Scientific Nexsa).

2.3. Sensor fabrication and evaluation

The prepared powder was mixed with deionized water to form a slurry which was spin-coated uniformly on an Au interdigital electrode, and after drying at RT for 8 h, the gas sensor was attained. The sensing properties are assessed at RT using a CGS-8 intelligent gas-sensitive analyzer system (25 °C, Beijing Zhongju Hi-Tech Co., Ltd., China). The response (S_g) is defined by the following **Equation (1)**:

$$S_g = \frac{|R_a - R_g|}{R_a} \quad (1)$$

where R_a and R_g represent the resistance of the sensor exposed to air and target gas, respectively. The response time and recovery time were defined as the time taken to reach 90 % of the total resistance change during adsorption and desorption, respectively.

2.4. DFT calculations

The calculations were performed by the Vienna Ab Initio simulation package based on density-functional theory (DFT) [21–23]. The

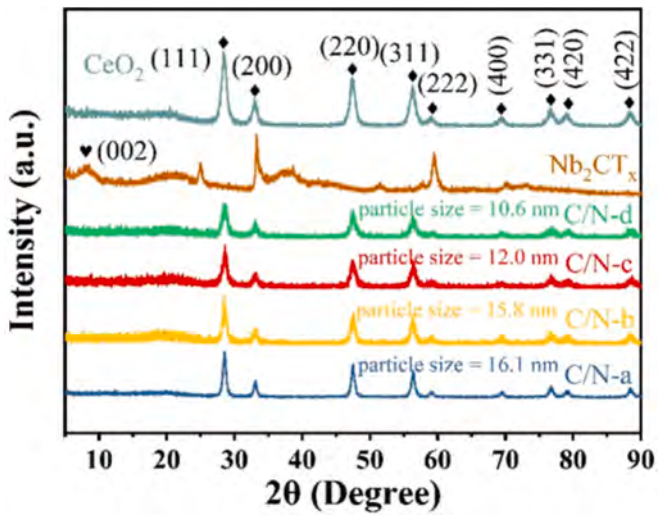

Fig. 2. XRD patterns of CeO_2, Nb_2CT_x, C/N-a, C/N-b, C/N-c, and C/N-d.

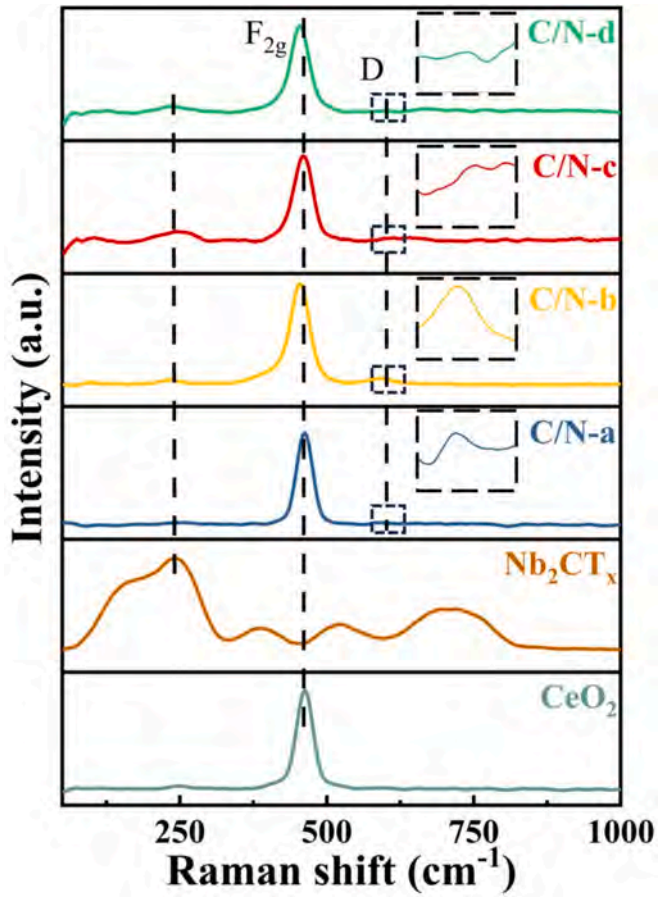

Fig. 3. Raman scattering spectra of CeO_2, Nb_2CT_x, C/N-a, C/N-b, C/N-c, and C/N-d.

exchange–correlation energy core electrons were described by the Perdew–Burke–Ernzerhof functional. The kinetic energy cutoff is set as 500 eV, and the Monkhorst–Pack scheme was employed to sample the Brillouin zone using a $3 \times 3 \times 1$ k-point grid for geometry optimization. The geometry was considered optimized when the force on each atom was smaller than 0.05 eV/Å. The adsorption energy is calculated as follows [24]:

$$E_{ads} = E_{total} - E_{gas} - E_{sub} \quad (2)$$

where E_{total}, E_{gas}, and E_{sub} are the energies of the adsorption system, gas molecule, and substrate, respectively. A more negative value means stronger adsorption.

3. Results and discussion

3.1. Materials characterization

Fig. 2 depicts the XRD patterns of CeO_2, Nb_2CT_x, and CeO_2/Nb_2CT_x composites. The diffraction peaks at angles (2θ) of 28.45°, 33.01°, 47.5°, 56.31°, 59.13°, 69.52°, 76.76°, 79.02°, and 88.51° correspond to the (111), (200), (220), (311), (222), (400), (331), (420), and (422) planes of CeO_2 [25], which are consistent with previous reports and can be indexed to the JCPDS card # 34–0394. The peak at 8° corresponds to the (002) planes of Nb_2CT_x [26], and no obvious diffraction peaks of Nb_2CT_x can be observed due to the small concentration of Nb_2CT_x in the composites. According to the Scherrer formula, the size of CeO_2 nanoparticles for the samples of C/N-a, C/N-b, C/N-c, and C/N-d are about 16.1 nm, 15.8 nm, 12.0 nm, and 10.6 nm, respectively. As the Nb_2CT_x content in the composites increases, the size of CeO_2 nanoparticles decreases. It indicates that the addition of Nb_2CT_x could effectively disrupt the stacking of CeO_2 nanoparticles during preparation, leading to reduction of grain size.

The Raman scattering spectra of CeO_2, Nb_2CT_x, and CeO_2/Nb_2CT_x composites are presented in Fig. 3. As the Nb_2CT_x content in the composite increases, the characteristic peak intensity of Nb_2CT_x at 249 cm^{-1} also increases [27]. The F_{2g} peak at 450 cm^{-1} corresponds to the fluorite phase of CeO_2, while the defect-induced (D) mode appears at 590 cm^{-1} [28]. No significant D peak was observed in CeO_2. The ratio of $I_D/I_{F_{2g}}$ is related to the concentration of oxygen vacancy (O_v) [29]. The higher ratio of $I_D/I_{F_{2g}}$ means the larger concentration of O_v. The composites with 0.5 wt% Nb_2CT_x (C/N-b) behaves the highest $I_D/I_{F_{2g}}$ value (0.0647), indicating that the C/N-b contains the highest concentration of O_v (Table S1).

The morphologies of Nb_2CT_x and CeO_2/Nb_2CT_x are examined by SEM and TEM. As shown in Fig. 4(a-c), the Nb_2CT_x behaves the smooth and accordion-like structure. After composited with CeO_2 nanoparticles, the surface of layered Nb_2CT_x becomes rough, indicating that the CeO_2 nanoparticles are deposited on the surface of Nb_2CT_x, forming the heterogeneous interfaces and providing abundant adsorption sites for gas adsorption (Fig. 4d and e). Fig. 4(f-j) shows the elemental map of CeO_2/Nb_2CT_x composites (C/N-b), revealing the Ce and O elements is uniformly distributed on the surface of Nb_2CT_x.

The TEM and HR-TEM images of Nb_2CT_x are depicted in Fig. 5(a-c). The Nb_2CT_x show the layered structure and the lattice spacing of 0.27 nm corresponds to the (042) plane of Nb_2CT_x. The selected-area electron diffraction (SAED) pattern in Fig. 5d display the Nb_2CT_x behaves the typical hexagonal crystalline structure. In Fig. 5e, the CeO_2 nanoparticles are deposited on the surface of Nb_2CT_x, and the lattice spacings of 0.28 and 0.32 nm correspond to the (200) and (1 1 1) planes of CeO_2 (Fig. 5(f-h)).

The XPS spectra of Nb_2CT_x are shown in Fig. 6(a-b). The Nb 3*d* peaks at 209.90/207.16 eV and 208.02/205.08 eV are assigned to Nb_2O_5 and Nb-C, respectively. Because the surface functional groups such as −O, −F, and –OH occurs on the surface of Nb atoms, the Nb atoms behave the +3 valence state [26]. In addition, the edges and structural defects of the MXene nanosheets are more susceptible to be oxidated, leading to formation of Nb_2O_5 and thus some Nb atoms behave the +5 valence state [30]. Fig. 6(c–f) presents the XPS spectra of the CeO_2/Nb_2CT_x composites. The survey XPS spectrum shows that the main elements in composites were Ce, Nb, C, F, and O, demonstrating the thorough etching of Al element from Nb_2AlC by HF solution (Fig. 6c). The Ce 3*d* XPS spectrum can be deconvoluted into eight peaks (Fig. 6d). The fitting peaks at

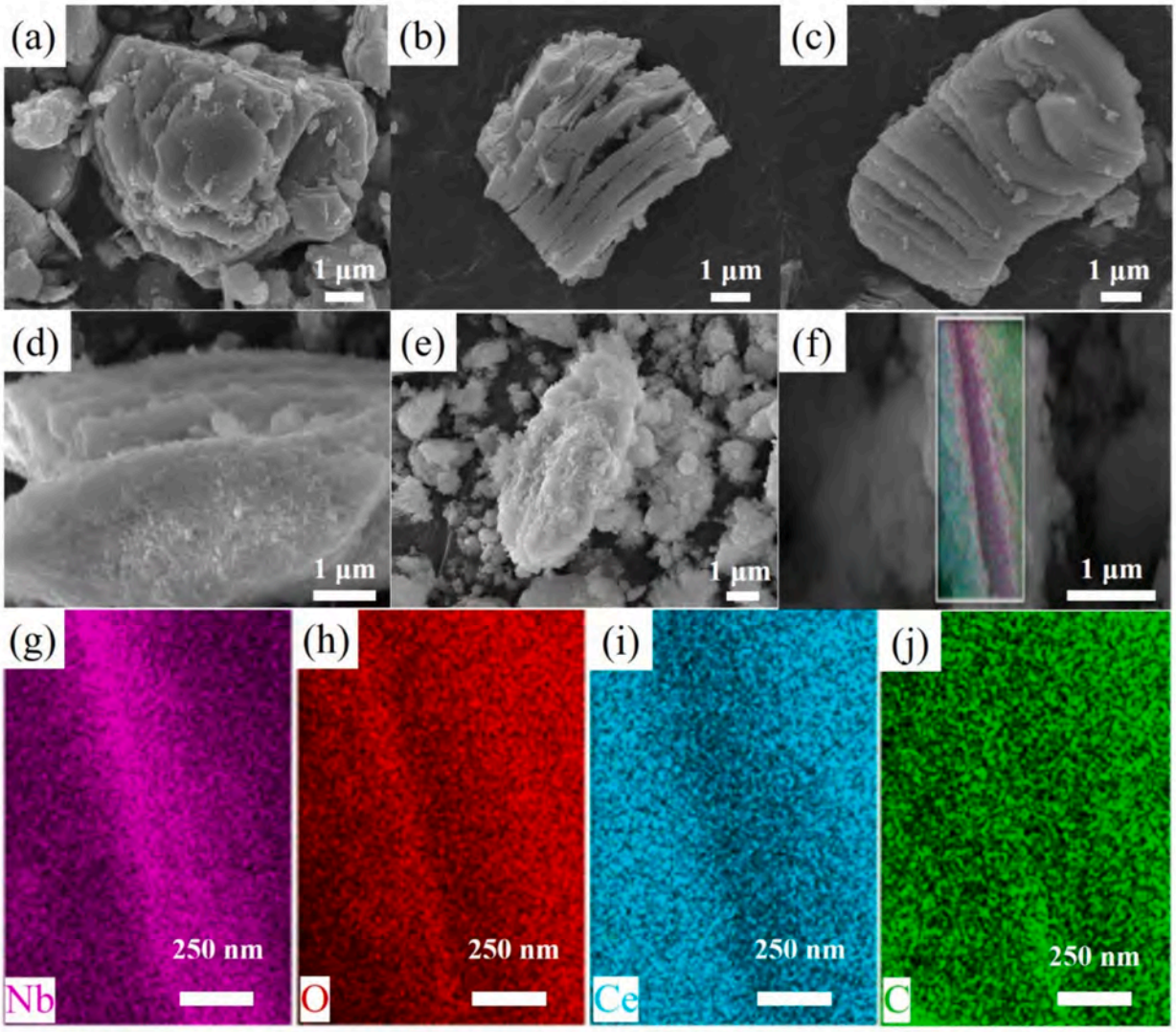

Fig. 4. SEM images of (a-c) Nb_2CT_x and (d-f) C/N-b; Elemental maps of (g) Nb, (h) O, (i) Ce, and (j) C.

about 901.26 eV (U), 903.09 eV (U′), 907.72 eV (U″) and 916.98 eV (U‴) represents the Ce $3d_{3/2}$ and the other fitting peaks at about 882.66 eV (V), 885.29 eV (V′), 889.36 eV (V″) and 898.66 eV (V‴) represents the Ce $3d_{5/2}$. Among them, the U′ and V′ peaks belong to the Ce^{3+} states, and the other peaks belong to the Ce^{4+} states [31]. For CeO_2, if the Ce^{3+} ion occurs, the oxygen vacancies (O_v) will be formed to attain charge neutrality. The reaction is shown in Equation (3) [32]:

$$2Ce^{4+} + O^{2-} \rightarrow 2Ce^{3+} + V_O + 0.5O_2 \quad (3)$$

where, the V_O represents the O_v. The higher density of Ce^{3+} ions indicate the larger concentration of O_v. The O 1*s* peaks at 531.45 eV, 529.63 eV, and 529.17 eV are assigned to the adsorbed oxygen (O_S) of CeO_2 nanocrystals, O_V, and lattice oxygen (O_L), respectively (Fig. 6e) [31]. The concentration of O_V is about 40.64 %. The Nb 3*d* peaks of Nb_2CT_x at about 209.61/206.78 eV and 208.49/204.98 eV are from Nb_2O_5 and Nb–C, respectively (Fig. 6f), and the Nb-O bond stems from the oxidation of Nb_2CT_x during the hydrothermal process [30]. After formation of composites, a slight shift toward lower binding energy is observed, indicating that the charge transfer occurs at interface, leading to formation of the heterogeneous interfaces.

To further confirm presence of the O_v, the electron paramagnetic resonance (EPR) spectra of CeO_2 and CeO_2/Nb_2CT_x composites were measured. As shown in Fig. 7, the EPR signal at g = 2.003 corresponds to unpaired electrons trapped at O_v sites, serving as a characteristic indicator of O_v formation[33]. Compared to pure CeO_2, the CeO_2/Nb_2CT_x composites exhibit the significantly stronger EPR signal at g-value, suggesting the higher concentration of O_v. This enhancement can be attributed to the interaction between Nb_2CT_x and CeO_2, which facilitates defect formation by modifying the electronic environment and thus promotes charge transfer. The increased O_v density in CeO_2/Nb_2CT_x composites could promote the adsorption of NH_3 molecular, enhancing the NH_3-sensing response.

To evaluate the specific surface area of samples, N_2 adsorption and desorption measurements were conducted for CeO_2 and CeO_2/Nb_2CT_x composites. As shown in Fig. 8, the specific surface areas of CeO_2 and Nb_2CT_x are 75.584 and 3.944 m^2/g, respectively. For the samples of C/N-a, C/N-b, C/N-c and C/N-d, the specific surface areas are 70.121, 87.127, 91.909, and 104.184 m^2/g, respectively. As the Nb_2CT_x content increases, the size of CeO_2 nanoparticles decreases, leading to a larger surface area. Although the surface area of C/N-b is smaller than that of C/N-c and C/N-d, the concentration of O_v is higher. Hence, the C/N-b behaves the highest room-temperature NH_3 sensing response.

3.2. Gas sensing properties

The room-temperature response of CeO_2, Nb_2CT_x and composites to 500 ppm NH_3 is displayed in Fig. 9a. The response of pure CeO_2 to 500

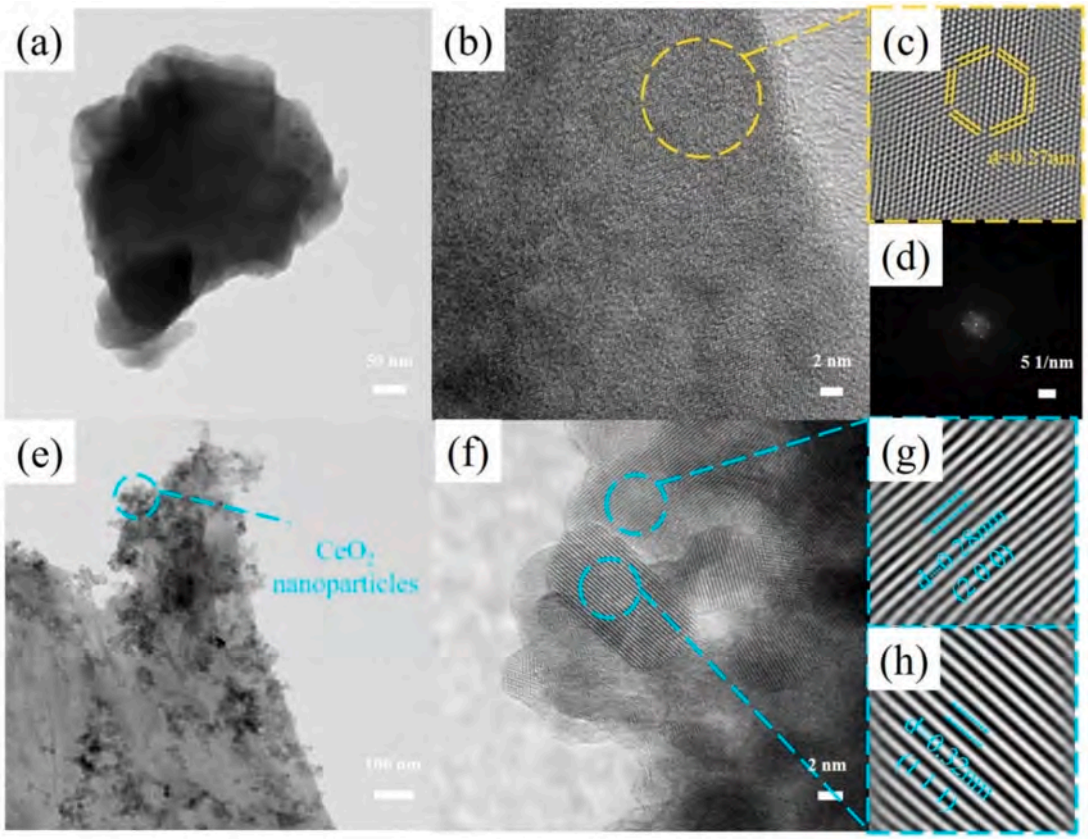

Fig. 5. TEM patterns of (a-c) Nb_2CT_x and (e-h) C/N-b at different magnifications; (d) Selected-area electron diffraction pattern of Nb_2CT_x.

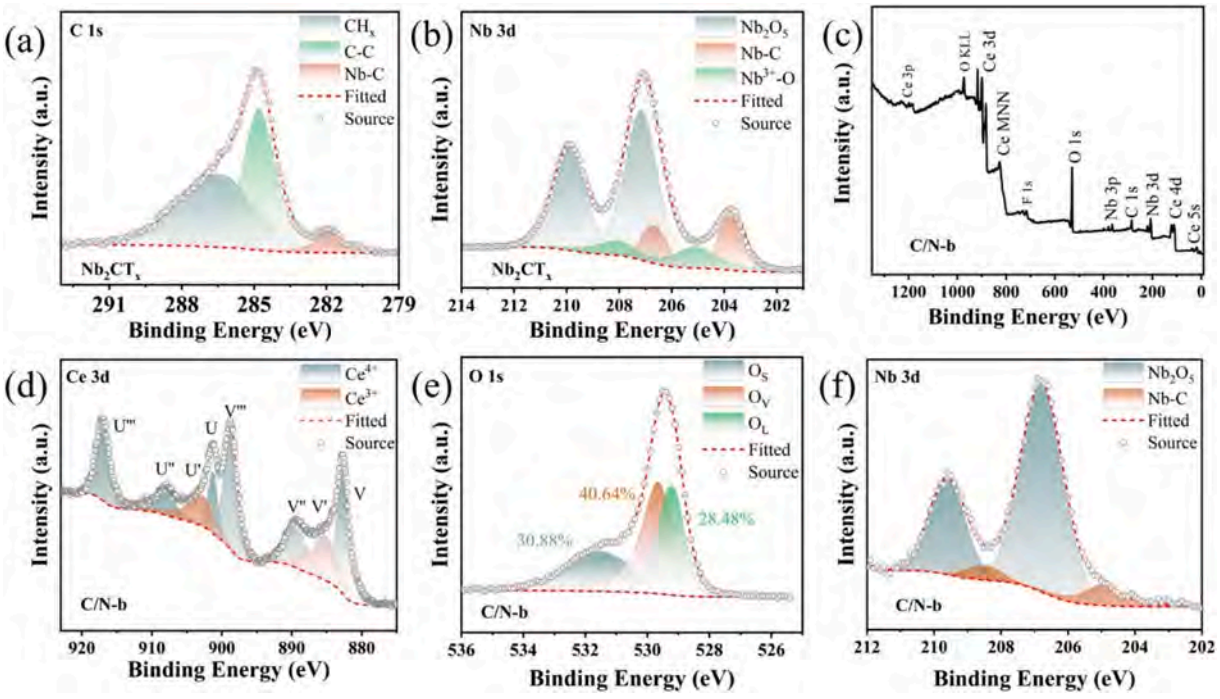

Fig. 6. XPS spectra of Nb_2CT_x and C/N-b: (a) C 1 *s*, and (b) Nb 3*d* of Nb_2CT_x. (c) Survey scan spectrum, (d) Ce 3*d*, (e) O 1 *s*, and (f) Nb 3*d* of C/N-b.

ppm NH_3 is about 18.5 %, which is much lower than that of Nb_2CT_x (62.4 %). The response of the CeO_2 and Nb_2CT_x composite rises initially and then declines with increasing Nb_2CT_x contents. Because the adsorption ability of Nb_2CT_x is lower than that of CeO_2. At a high concentration, the adsorption ability for NH_3 becomes worse. Among the various samples, the composites with 0.5 wt% Nb_2CT_x has the best sensing properties. In addition, according to the results of BET, the specific surface area of C/N-b is only 15 % higher than that of CeO_2.

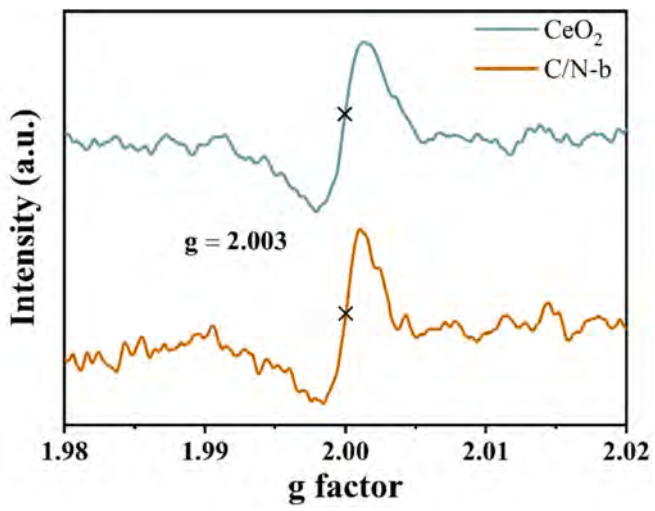

Fig. 7. EPR spectra of CeO_2 and C/N-b.

While, the room-temperature NH_3 sensing response is significantly enhanced by 4 times. In fact, the enhanced NH_3 sensing response of composite is attributed to the multiple factors. Except for specific surface area, the enhanced NH_3 sensing response is also depended on the O_v. According to the results of Raman and EPR, incorporation of Nb_2CT_x could promote formation of O_v in CeO_2. The O_v could serve as the highly active sites, promoting adsorption and reaction of NH_3 molecular on the surface of sensor. With increase of Nb_2CT_x content, the concentration of O_v is increased firstly and then decreased. The composites with 0.5 wt% Nb_2CT_x possesses high concentration of O_v and behaves the highest NH_3-sensing response. Fig. 9(b-d) present the resistance changes to 500 ppm NH_3 at RT. The resistance of CeO_2, Nb_2CT_x, and composites decreases and shows n-type semiconducting properties [26]. The Hall effect of CeO_2 and Nb_2CT_x composites (C/N-b) is measured and the Hall coefficient is $-4092.001\ cm^3/C$. The majority carrier in the composites is electrons, confirming the n-type semiconducting behavior. Upon exposure to air, the resistance recovers gradually back to the initial value. Although the response time of pure CeO_2 is about 283 s, which is longer than that of Nb_2CT_x (108 s), the recovery time of CeO_2 (234 s) is shorter than that of Nb_2CT_x (568 s). As for the composite, the response at RT is obviously enhanced. Fig. 9e shows the real-time resistance changes of C/N-b to different concentrations of NH_3. With increasing NH_3 concentration, the room-temperature response becomes better. Meanwhile, the recovery time also increases. The response/recovery times are about 118 s/978 s, 12 s/565 s, 83 s/300 s, and 119 s/314 s for 500 ppm, 300 ppm, 100 ppm, and 50 ppm NH_3, respectively (Fig. 9f). In general, the response time decreases as the concentration of detected gas increases. However, in this paper, the response time decreases when the NH_3 concentration is increased form 50 to 300 ppm and then increases as the NH_3 concentration is further increased. At low NH_3 concentration, the small amount of NH_3 molecular are adsored on the surface of sensor, resultting the poor reaction rate between NH_3 molecular and surface-adsorbed oxygen. Hence, the response time is longer. As the concentration of NH_3 increases, the NH_3 molecules diffuse more rapidly to the surface of sensor, accelerating the adsorption and reaction rates. Hence, the resistance of sensor could attain the stable state quickly, behaving the lower response time. While, as the NH_3 concentration is further increased, the active sites are all occupied by NH_3 molecular, reaching the saturated state. The dense NH_3 molecular layer is formed, hindering the diffusion of additional NH_3 molecules into the inner layer of sensor, leading to the increase of response time. The response of C/N-b to 10 ppm, 1 ppm and 500 ppb NH_3 was tested and the results are shown in Fig. S1. The response to 10 ppm, 1 ppm and 500 ppb NH_3 are about 9.6 %, 2.5 % and 1.2 %, respectively. Additionally, the lowest detection limit (LOD) of C/N-b was calculated and the process of calculation is presented in Fig. S2 and Table S2. The theoretical LOD of C/N-b is about 3.88 ppb, which indicates the CeO_2 and Nb_2CT_x composites behave the promissing potential for detecting low concentrations of NH_3 at RT.

The repeatability is shown in Fig. 9g. The output resistance stabilizes after four cycles, and the relative standard deviation (RSD) of the response is 1.95 % for 100 ppm NH_3 at RT, indicating outstanding reversibility and repeatability. The long-term stability is also evaluated. As shown in Fig. S3, the RSD of response is 4.5 %, indicating excellent stability of the sensor. The 500 ppm NH_3 sensing response of C/N-b at different humidity is presented in Fig. 9h. The response decreases as the relative humidity increases from 60 % to 90 % at RH due to partial occupation of water molecules of the sensing sites, resulting in the poor

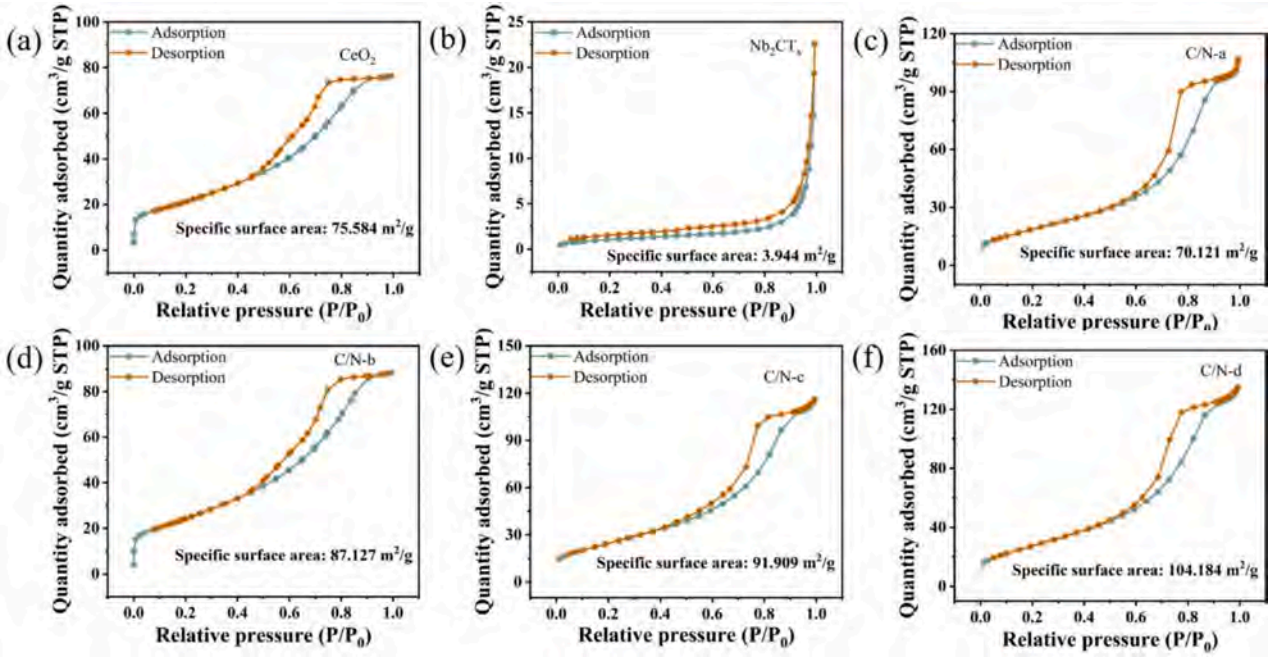

Fig. 8. N_2 adsorption–desorption isotherms of CeO_2, Nb_2CT_x, C/N-a, C/N-b, C/N-c, and C/N-d.

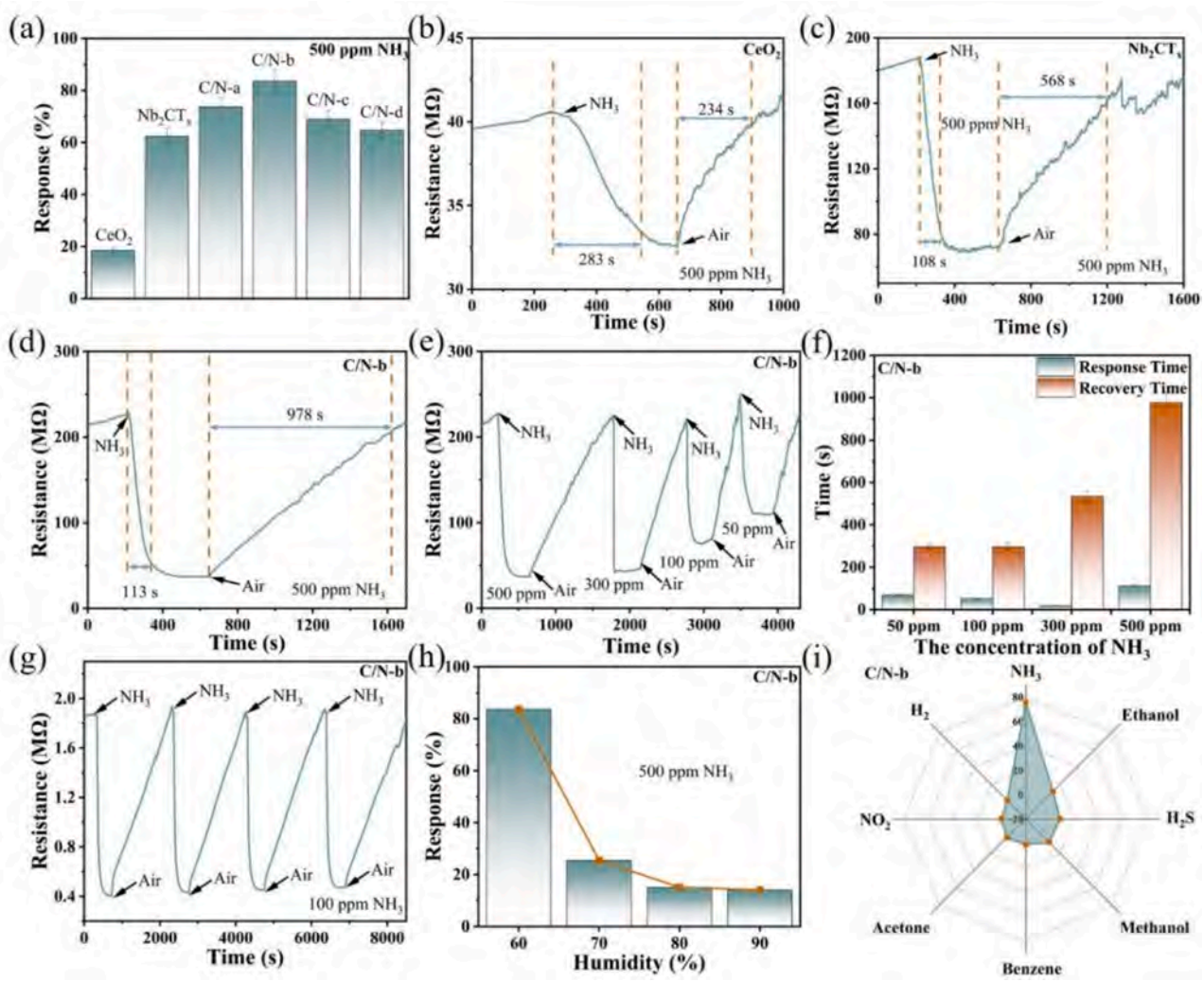

Fig. 9. (a) Sensitivity of CeO_2, Nb_2CT_x, C/N-a, C/N-b, C/N-c, and C/N-d for 500 ppm NH_3 at RT; (b-d) Dynamic response-recovery curves of CeO_2, Nb_2CT_x, and C/N-b for 500 ppm NH_3 at RT; (e) Dynamic response-recovery curves of C/N-b for different concentrations of NH_3 at RT; (f) Response time and recovery time of C/N-b for different concentrations of NH_3 at RT; (g) Response of C/N-b to 100 ppm NH_3 for 4 cycles at RT; (h) Response of C/N-b to 500 ppm NH_3 at different humidity levels at RT; (i) Selectivity to NH_3 of C/N-b in the presence of 100 ppm Ethanol, H_2S, Methanol, Benzene, Acetone, NO_2 and H_2 at RT.

NH_3 sensing response at high relative humidity. To evaluate the selectivity of CeO_2/Nb_2CT_x composites, the response to 100 ppm of NH_3, ethanol, H_2S [25], methanol, benzene, acetone, NO_2 and H_2 [25] were tested. As shown in Fig. 9i, the response to 100 ppm NH_3 is significantly higher than that of other interfering gases, demonstrating excellent selectivity. Based on the theory of Knudsen diffusion, the diffusion rate of the gas can be correlated to the molecular weight. The Knudsen diffusion constant (D_K) is defined as:

$$D_K = \frac{3r}{4}\sqrt{\frac{2RT}{\pi M}} \tag{4}$$

where r, R, T, and M are the pore radius, gas constant, temperature, and gas mass, respectively. For the acetone, benzene, methanol, ethanol and NO_2 gas molecules, the molecular weight is higher than that of NH_3. The Knudsen diffusion constant is smaller than that of NH_3, resulting in lower response than that of NH_3. For the H_2, the molecular weight is smaller than that of NH_3 and thus the Knudsen diffusion constant is higher. While, the adsorption ability of CeO_2 toward H_2 is much poorer

Table 1
Comparison of this work with other recently reported CeO_2-based and Nb_2CT_x-based NH_3 sensors.

Materials	Work temperature (℃)	Concentration (ppm)	Sensitivity (%)	Response /recovery time (s)	Reference
CeO_2/SiO_2 composites	RT	40	1700	312/1875	[15]
$CeO_2/MoSe_2$ composites	RT	5	61.8	73/300	[34]
CeO_2/PANI composites	RT	50	260	360/780	[35]
CeO_2/MWCNT composite	RT	5	5	110/150	[36]
CeO_2/ZnO composites	300	24	45.48	35/37	[37]
Nb_2CT_x/PANI composites	RT	50	205.39	530/660	[26]
$Nb_2CTx/MoSe_2$ composites	RT	50	71	14.7/20.1	[38]
CeO_2/Nb_2CT_x composites	**RT**	**50**	**51.2**	**70/298 s**	**This work**

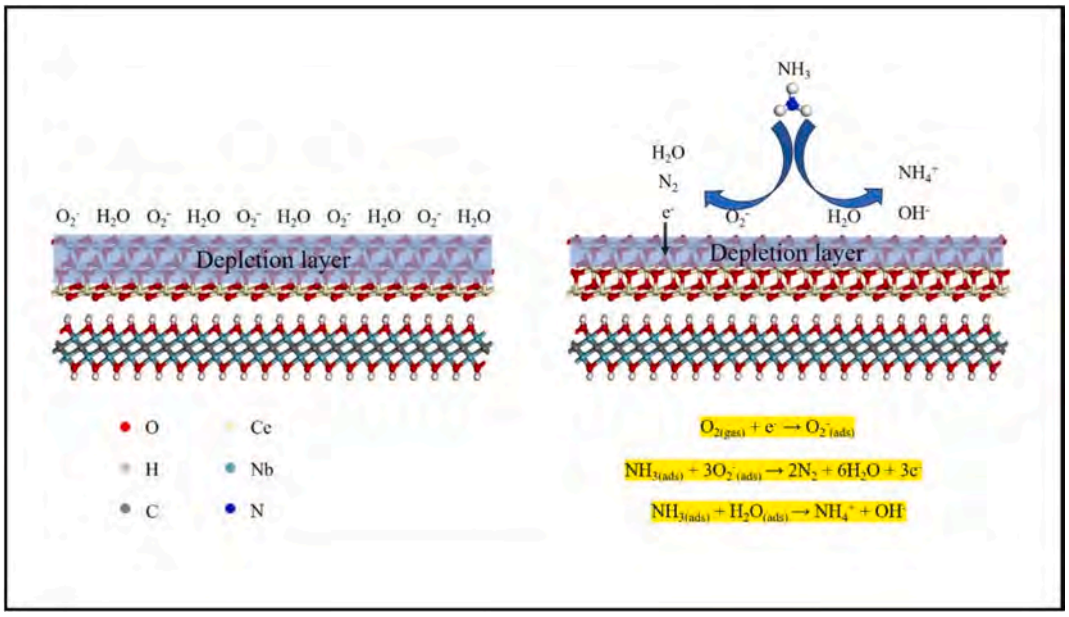

Fig. 10. Gas-sensing mechanism of CeO_2 and Nb_2CT_x composites for NH_3.

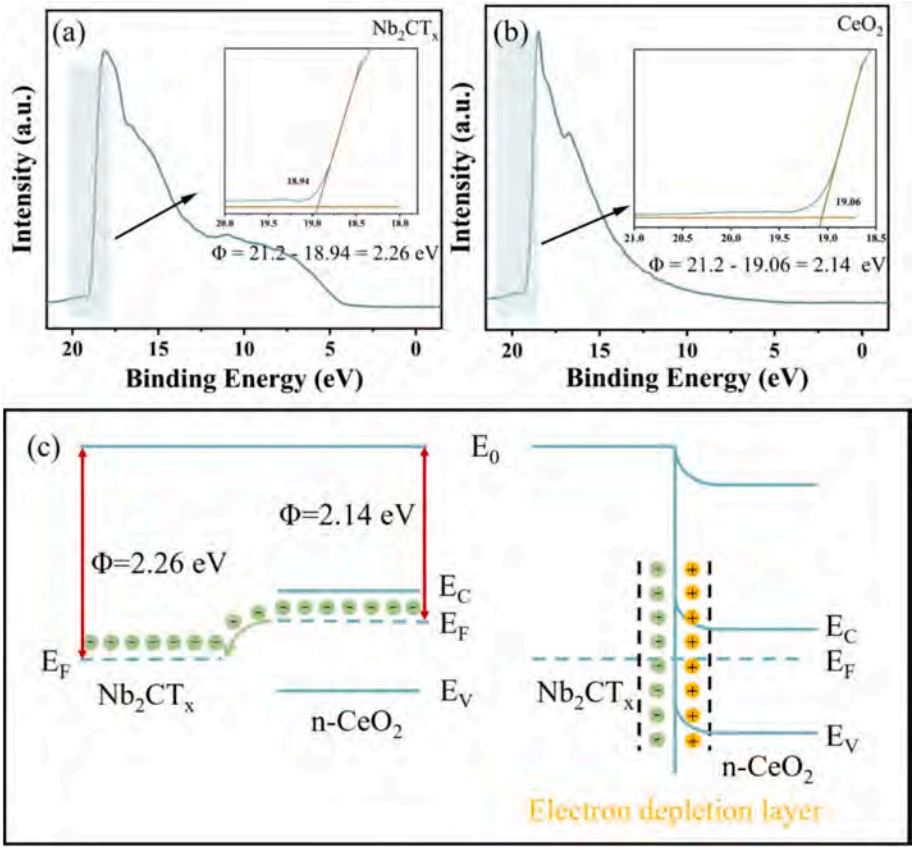

Fig. 11. UPS spectra of (a-b) Nb_2CT_x and CeO_2; (c) Work functions of CeO_2 and Nb_2CT_x.

than that of NH_3 (Fig. S4), resulting in the lower response. For the C_2H_6O and NO_2, they have the same molecular weight of 46 and thus have the same Knudsen diffusion constant. But, the adsorption ability of CeO_2 toward C_2H_6O and NO_2 molecular is different, behaving the different sensing response.

The results of this work and the previous reported work were collected and summarized in Table 1. Compared to previously reported CeO_2-based and Nb_2CT_x-based sensors, the C/N-b sensor in this work exhibits significantly lower response and recovery times than CeO_2/PANI, Nb_2CT_x/PANI, and CeO_2/SiO_2 composites. The recovery time is decreased by 80.21 %, compared to CeO_2/PANI composites. Although the response of this work is comparable to that of CeO_2/MWCNT composites, the recovery time is lower. For the CeO_2/ZnO composites, the work temperature is higher, resulting the high energy consumption. The

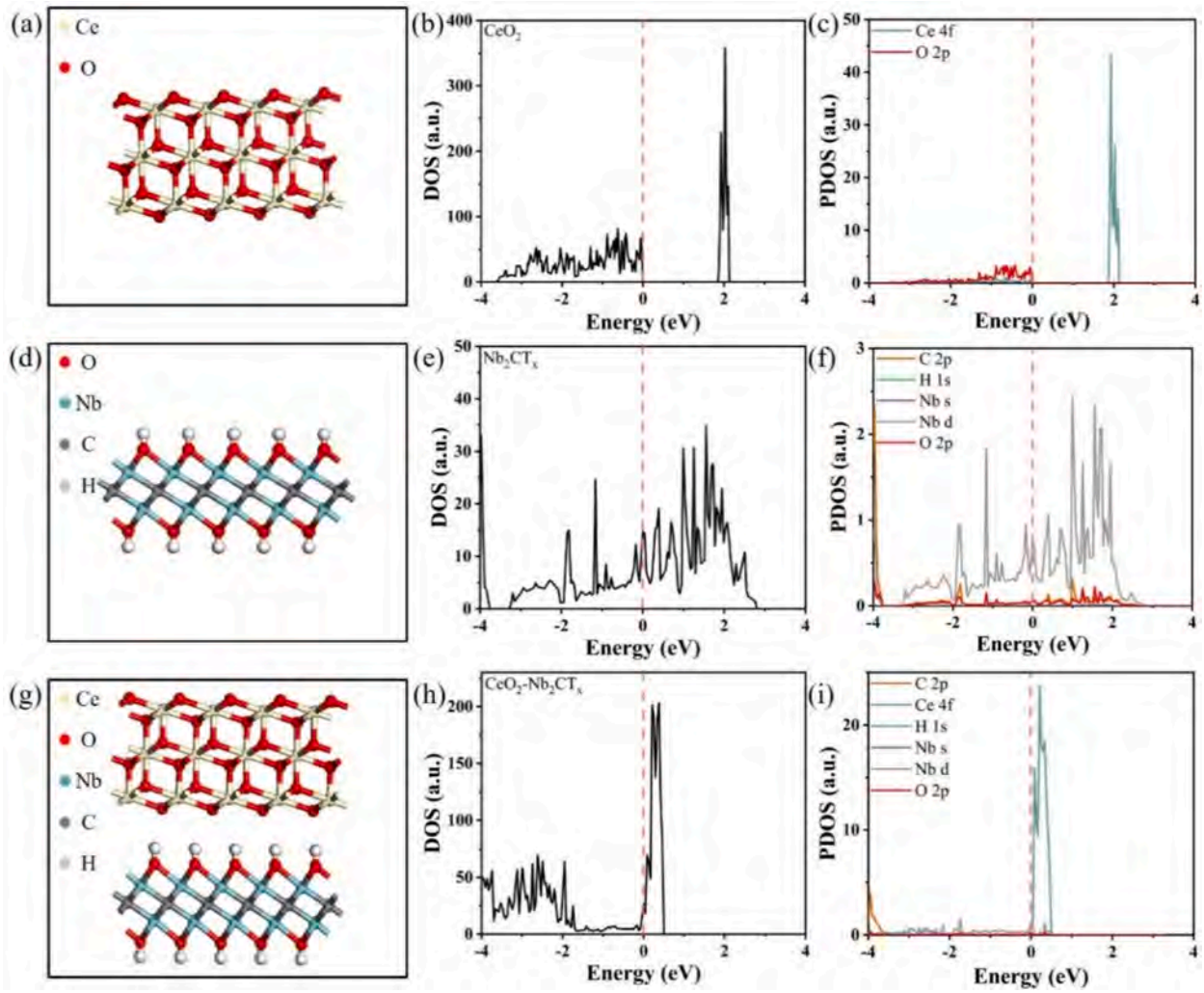

Fig. 12. Crystal structure, DOS, and PDOS of (a-c) CeO_2, (d-f) Nb_2CT_x, and (g-i) CeO_2 and Nb_2CT_x composites.

CeO_2/$MoSe_2$ composites demonstrate higher response, lower response and recovery time. While, besides NH_3, it also behaves the higher response of 58 % to 1 ppm TEA, showing the poor selectivity. In summary, the CeO_2 and Nb_2CT_x composites in this work show the excellent NH_3 sensing performance at RT.

3.3. Gas sensing mechanism

The underlying mechanism of CeO_2 and Nb_2CT_x is proposed in Fig. 10. In air, oxygen absorbs on the surface of CeO_2 and traps electrons from the conduction band to form chemisorbed oxygen species (O_2^-). In NH_3, NH_3 reacts with adsorbed oxygen to inject electrons back into the conduction band, thereby lowering the resistance (**Eq.5–7**) [39]. In addition, NH_3 may react with H_2O to generate NH_4^+ and OH^- ions to reduce the resistance (**Eq.** (8).

$$O_2(ads) + e^- \rightarrow O_2^-(ads) \tag{5}$$

$$NH_3(gas) \rightarrow NH_3(ads) \tag{6}$$

$$4NH_3(ads) + 3O_2^-(ads) \leftrightarrow 2N_2 + 6H_2O + 3e^- \tag{7}$$

$$NH_3(ads) + H_2O \leftrightarrow NH_4^+ + OH^- \tag{8}$$

The work function of CeO_2 and Nb_2CT_x are determined by UPS. As shown in Fig. 11, the work function of Nb_2CT_x is 2.26 eV, which is larger than that of CeO_2 (2.14 eV). When CeO_2 is in contact with Nb_2CT_x, electrons move from CeO_2 to Nb_2CT_x until the Fermi level equilibrates. The energy band of CeO_2 bends upward to form a Schottky barrier at the interface. The current passing through the Schottky barrier can be calculated by the following equations (9) and (10):

$$I_{TE} = SA^*T^2\exp\left(-\frac{q\varphi_{SB}}{kT}\right)\left[\exp\left(\frac{qv}{kT}-1\right)\right] \tag{9}$$

and

$$A^* = \frac{4\pi q m^* k^2}{h^3} \tag{10}$$

The depletion layer width can be calculated as:

$$W_D = \sqrt{\frac{2\varepsilon_s}{qN_D}\left(V_{bi} - V - \frac{kT}{q}\right)} \tag{11}$$

where S is the Schottky contact area, A^* is the effective Richardson constant, T is the temperature, q is the unit electronic charge, k is Boltzmann's constant, V is the applied voltage, φ_{SB} is the Schottky barrier height, V_{bi} is the built-in potential, and ε_s is the permittivity. In NH_3, the electrons of NH_3 are released back to the conduction band of CeO_2. The built-in potential decreases to narrow the electron depletion layer. The current passing through the interface increases, resulting in higher conductivity and better NH_3 sensing response at RT. Moreover, the current passing through the Schottky contact is sensitive to the Schottky barrier height (SBH). A bigger SBH translates into poor

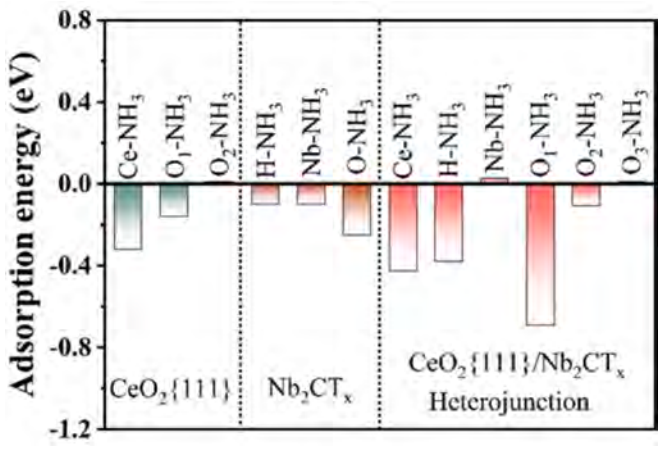

Fig. 13. Adsorption energies of NH_3 on the surface of CeO_2, Nb_2CT_x and CeO2/Nb_2CT_x heterojunction.

electron transfer at the interface and gas-sensing response. In principle, the SBH is mainly dependent on the difference of the work functions between the metal oxide and MXene. UPS reveals that the work function difference between CeO_2 and Nb_2CT_x is only 0.12 eV, indicative of a small SBH. It is thus easier for electrons to traverse the interface for better NH_3 sensing.

To further investigate the mechanism, the density of states and adsorption energy are calculated by first-principles calculation. Fig. 12 shows the total density of states (DOS) and projected density of states (PDOS) of CeO_2, Nb_2CT_x, and the composite. The valence band top and conduction band bottom of CeO_2 are mainly dominated by O 2*p* and Ce 4*f* states, respectively. The bandgap is about 1.8 eV (Fig. 12(a-c)). Hence, electrons transfer from the valence band to the conduction band is hindered at RT [40], resulting in a lower response to NH_3 at RT. As for Nb_2CT_x, the valence band overlaps the conduction band at the Fermi level showing metallic characteristics. Electrons move from the valence band to the conduction band easily. After the heterojunction of CeO_2 and Nb_2CT_x is formed, the valence band and conduction band overlap at the interface giving rise to metallic properties. Electrons move from CeO_2 to Nb_2CT_x easily, leading to excellent NH_3 sensing response at RT.

The adsorption structure and adsorption energy of NH_3 on the surface of CeO_2, Nb_2CT_x and CeO_2/Nb_2CT_x heterojunction are calculated and shown in Fig. S5 and Fig. 13. The CeO_2 has a higher adsorption energy for NH_3 compared to Nb_2CT_x. Hence, CeO_2 nanoparticles serve as the main adsorption sites for NH_3 and Nb_2CT_x provides the main conduction path. When the heterojunction of CeO_2 and Nb_2CT_x is formed, the adsorption energy is much more negative than that of pure CeO_2 and Nb_2CT_x. Hence, introduction of CeO_2 nanoparticles on the surface of Nb_2CT_x could improve the density of active sites for NH_3 adsorption and enhance NH_3-sensing response at RT. In addition, the adsorption distances are also calculated and the results are shown in Fig. S6. It's found that the adsorption distance of CeO_2 and Nb_2CT_x heterojunction is smaller than that of pure CeO_2 and Nb_2CT_x at the same adsorption site. In general, the stronger adsorption ability means the lower adsorption distance. Hence, it further confirmed that introduction of CeO_2 nanoparticles on the surface of Nb_2CT_x could improve the adsorption ability of NH_3 molecular.

4. Conclusion

The composites of CeO_2 and Nb_2CT_x are synthesized hydrothermally. The Nb_2CT_x serves as the substrate for Ce^{3+} ions adsorption, reaction, nucleation, and then growth of CeO_2 nanoparticles. During NH_3-sensing response, the Nb_2CT_x mainly serves as the underlying layer, providing the efficient channels for electron transport at RT and the CeO_2 nanoparticles mainly provides the active sites for NH_3 adsorption. The room-temperature NH_3-sensing response initially increases and then decreases with increasing Nb_2CT_x content. Compared to pure CeO_2, the response of composite of CeO_2 and Nb_2CT_x toward 500 ppm NH_3 is enhanced by 4 times, along with the short response and recovery times, long-term stability, and low detection limit. First-principles calculation reveal that CeO_2 and Nb_2CT_x heterojunction has more negative adsorption energy for NH_3 than CeO_2 and Nb_2CT_x, indicating that CeO_2 on the Nb_2CT_x surface could enhance NH_3 adsorption. The heterojunction of CeO_2 and Nb_2CT_x at interface increases the carrier lifetime and exposes more active sites for NH_3 adsorption, ultimately resulting in better room-temperature NH_3 detection.

CRediT authorship contribution statement

Dingyuan Wang: Writing – review & editing, Writing – original draft, Data curation. **Lizhai Zhang:** Writing – review & editing, Project administration, Funding acquisition. **Jiayuan Xu:** Supervision. **Xinyu Lei:** Supervision. **Henghui Sun:** Supervision. **Fei Ma:** Supervision. **Taotao Ai:** Supervision, Funding acquisition. **Paul K. Chu:** Writing – review & editing, Supervision.

Declaration of competing interest

The authors declare that they have no known competing financial interests or personal relationships that could have appeared to influence the work reported in this paper.

Acknowledgments

This work was jointly supported by the National Natural Science Foundation of China (grant no. 51771144), Natural Science Foundation of Shaanxi Province (2023-JC-QN-0476), Shaanxi University of Technology Research Grant (no. SLGRCQD2207), Scientific research project of Shaanxi Provincial Education Department (no.23JK0375), Science and technology program for overseas students of Shaanxi province (2023016), and City University of Hong Kong Donation Research Grants (nos. DON-RMG 9229021 and 9220061).

Appendix A. Supplementary data

Supplementary data to this article can be found online at https://doi.org/10.1016/j.cej.2025.162687.

Data availability

The authors are unable or have chosen not to specify which data has been used.

References

[1] H.S. Kim, J. Choi, J. Kong, H. Kim, S.J. Yoo, H.S. Park, Regenerative electrocatalytic redox cycle of copper sulfide for sustainable NH_3 production under ambient conditions, ACS Catal. 11 (1) (2021) 435–445, https://doi.org/10.1021/acscatal.0c03985.
[2] W.-J. Jiang, J.-B. Zhang, Y.-T. Zou, H.-L. Peng, K. Huang, Manufacturing acidities of hydrogen-bond donors in deep eutectic solvents for effective and reversible NH_3 capture, ACS Sustain. Chem. Eng. 8 (35) (2020) 13408–13417, https://doi.org/10.1021/acssuschemeng.0c04215.
[3] S. Aarya, Y. Kumar, R.K. Chahota, Recent advances in materials, parameters, performance and technology in ammonia sensors: A review, J. Inorg. Organomet. Polym. Mater. 30 (2) (2020) 269–290, https://doi.org/10.1007/s10904-019-01208-x.
[4] A.G. Bannov, M.V. Popov, A.E. Brester, P.B. Kurmashov, Recent advances in ammonia gas sensors based on carbon nanomaterials, Micromachines 12 (2) (2021) 186, https://doi.org/10.3390/mi12020186.
[5] X. Tang, M. Debliquy, D. Lahem, Y. Yan, J.-P. Raskin, A review on functionalized graphene sensors for detection of ammonia, Sensors 21 (4) (2021) 1443, https://doi.org/10.3390/s21041443.
[6] P. Li, B. Wang, C. Qin, C. Han, L. Sun, Y. Wang, Band-gap-tunable CeO_2 nanoparticles for room-temperature NH_3 gas sensors, Ceram. Int. 46 (11, Part B) (2020) 19232–19240. https://doi.org/10.1016/j.ceramint.2020.04.261.

[7] Y. Fu, T. Wang, X. Wang, X. Li, Y. Zhao, F. Li, G. Zhao, X. Xu, Investigation of p-n sensing transition and related highly sensitive NH_3 gas sensing behavior of SnPx/rGO composites, Chem. Eng. J. 471 (2023) 144499, https://doi.org/10.1016/j.cej.2023.144499.

[8] Q. Li, W. Zeng, Y. Li, Metal oxide gas sensors for detecting NO_2 in industrial exhaust gas: Recent developments, Sens. Actuators B Chem. 359 (2022) 131579, https://doi.org/10.1016/j.snb.2022.131579.

[9] L. Chen, Z. Liu, Z. Guo, X.-J. Huang, Regulation of intrinsic physicochemical properties of metal oxide nanomaterials for energy conversion and environmental detection applications, J. Mater. Chem. A 8 (34) (2020) 17326–17359, https://doi.org/10.1039/D0TA05539E.

[10] M. Dadkhah, J.-M. Tulliani, Green synthesis of metal oxides semiconductors for gas sensing applications, Sensors 22 (13) (2022) 4669, https://doi.org/10.3390/s22134669.

[11] R. Ramanathan, S. Nagarajan, V. Bonu, P. Patel, S. Jamdar, H.C. Barshilia, R. C. Mallik, Enhanced sensing performance of Sb-doped nanometer-thin SnO_2 films toward CO and NH_3 gases, ACS Appl. Nano Mater. 6 (9) (2023) 7873–7886, https://doi.org/10.1021/acsanm.3c01032.

[12] H. Yu, L. Dai, Y. Liu, Y. Zhou, P. Fan, J. Luo, A. Zhong, $Ti_3C_2T_x$ MXene-SnO_2 nanocomposite for superior room temperature ammonia gas sensor, J. Alloys Compd. 962 (2023) 171170, https://doi.org/10.1016/j.jallcom.2023.171170.

[13] K.-P. Yuan, L.-Y. Zhu, J.-H. Yang, C.-Z. Hang, J.-J. Tao, H.-P. Ma, A.-Q. Jiang, D. W. Zhang, H.-L. Lu, Precise preparation of WO_3@SnO_2 core-shell nanosheets for efficient NH_3 gas sensing, J. Colloid Interface Sci. 568 (2020) 81–88, https://doi.org/10.1016/j.jcis.2020.02.042.

[14] D.D. Megersa, H.H. Cho, Y. Kim, G.T. Gudena, J. Lee, J.S. Bae, S. Chae, H.K. Yu, Position-selective growth of WO_3 nanosheets for NH_3 gas sensors, Cryst. Growth Des. 23 (5) (2023) 3447–3454, https://doi.org/10.1021/acs.cgd.3c00005.

[15] J. Wang, Z. Li, S. Zhang, S. Yan, B. Cao, Z. Wang, Y. Fu, Enhanced NH_3 gas-sensing performance of silica modified CeO_2 nanostructure based sensors, Sens. Actuators B Chem. 255 (2018) 862–870, https://doi.org/10.1016/j.snb.2017.08.149.

[16] D.E. Motaung, Z.P. Tshabalala, P.R. Makgwane, F.A. Mahmoud, D.N. Oosthuizen, F.R. Cummings, N. Leshabane, N. Hintsho-Mbita, X. Li, S.S. Ray, H.C. Swart, Multi-functioning of CeO_2-SnO_2 heterostructure as room temperature ferromagnetism and chemiresistive sensors, J. Alloys Compd. 906 (2022) 164317, https://doi.org/10.1016/j.jallcom.2022.164317.

[17] T. Hang, J. Wu, S. Xiao, B. Li, H. Li, C. Yang, C. Yang, N. Hu, Y. Xu, Y. Zhang, X. Xie, Anti-biofouling NH_3 gas sensor based on reentrant thorny ZnO/graphene hybrid nanowalls, Microsyst. Nanoeng. 6 (1) (2020) 41, https://doi.org/10.1038/s41378-020-0151-5.

[18] P. Nakarungsee, S. Srirattanapibul, C. Issro, I.M. Tang, S. Thongmee, High performance Cr doped ZnO by UV for NH_3 gas sensor, Sens. Actuators A Phys. 314 (2020) 112230, https://doi.org/10.1016/j.sna.2020.112230.

[19] S.K. Sinha, B. Kumar, R. Kumar, S. Ganguly, A. Hazra, Synthesis and characterization of hybrid NiO/CeO_2 p-n heterojunction nanofibers for room temperature ammonia sensing application, Surf. Interfaces 51 (2024) 104568, https://doi.org/10.1016/j.surfin.2024.104568.

[20] L. Wang, H. Huang, S. Xiao, D. Cai, Y. Liu, B. Liu, D. Wang, C. Wang, H. Li, Y. Wang, Q. Li, T. Wang, Enhanced sensitivity and stability of room-temperature NH_3 sensors using core-shell CeO_2 nanoparticles@cross-linked PANI with p-n heterojunctions, ACS Appl. Mater. Interfaces 6 (16) (2014) 14131–14140, https://doi.org/10.1021/am503286h.

[21] G. Kresse, J. Furthmüller, Efficiency of ab-initio total energy calculations for metals and semiconductors using a plane-wave basis set, Comput. Mater. Sci. 6 (1) (1996) 15–50, https://doi.org/10.1016/0927-0256(96)00008-0.

[22] J.P. Perdew, K. Burke, M. Ernzerhof, Generalized gradient approximation made simple, PhysRevLett.7 77 (18) (1996) 3865–3868, https://doi.org/10.1103/PhysRevLett.77.3865.

[23] G. Kresse, J. Furthmüller, Efficient iterative schemes for ab initio total-energy calculations using a plane-wave basis set, PhysRevB 54 (16) (1996) 11169–11186, https://doi.org/10.1103/PhysRevB.54.11169.

[24] T. Xie, X.-D. Wang, M. Yao, X.-S. Liu, Y.-G. Chen, First-principle study of CO adsorption and oxidation on Sm-doped CeO_2(111) surface, RSC Adv. 6 (24) (2016) 20349–20356, https://doi.org/10.1039/C5RA27890B.

[25] L. Zhang, J. Xu, X. Yang, X. Lei, H. Sun, Y. Huang, H. Lu, T. Ai, F. Ma, P.K. Chu, Edge-enriched CeO_2/MoS_2 heterostructure with coupled interface for enabling selective room-temperature NO_2 detection, Sens. Actuators B Chem. 419 (2024) 136443, https://doi.org/10.1016/j.snb.2024.136443.

[26] S. Wang, Y. Jiang, B. Liu, Z. Duan, H. Pan, Z. Yuan, G. Xie, J. Wang, Z. Fang, H. Tai, Ultrathin Nb_2CT_x nanosheets-supported polyaniline nanocomposite: Enabling ultrasensitive NH_3 detection, Sens. Actuators B Chem. 343 (2021) 130069, https://doi.org/10.1016/j.snb.2021.130069.

[27] Z. Yuan, L. Wang, D. Li, J. Cao, W. Han, Carbon-reinforced Nb_2CT_x MXene/MoS_2 nanosheets as a superior rate and high-capacity anode for sodium-ion batteries, ACS Nano 15 (4) (2021) 7439–7450, https://doi.org/10.1021/acsnano.1c00849.

[28] H. Xie, L. Mao, J. Mao, Structural evolution of Ce[Fe(CN)$_6$] and derived porous Fe-CeO_2 with high performance for supercapacitor, Chem. Eng. J. 421 (2021) 127826, https://doi.org/10.1016/j.cej.2020.127826.

[29] A.S. Mokrushin, E.P. Simonenko, N.P. Simonenko, K.A. Bukunov, V. G. Sevastyanov, N.T. Kuznetsov, Gas-sensing properties of nanostructured CeO_2-xZrO_2 thin films obtained by the sol-gel method, J. Alloys Compd. 773 (2019) 1023–1032, https://doi.org/10.1016/j.jallcom.2018.09.274.

[30] W. Wang, Y. Yao, J. Xin, X. Zhao, L. Xie, Z. Zhu, Room-temperature highly sensitive triethylamine detection by few-layer Nb_2CT_x MXene nanosheets, Nanotechnology 35 (21) (2024) 215502, https://doi.org/10.1088/1361-6528/ad2b4a.

[31] H. Bi, L.-X. Zhang, Y. Xing, P. Zhang, J.-J. Chen, J. Yin, L.-J. Bie, Morphology-controlled synthesis of CeO_2 nanocrystals and their facet-dependent gas sensing properties, Sens. Actuators B Chem. 330 (2021) 129374, https://doi.org/10.1016/j.snb.2020.129374.

[32] L. Zhang, Q. Fang, Y. Huang, K. Xu, P.K. Chu, F. Ma, Oxygen vacancy enhanced gas-sensing performance of CeO_2/graphene heterostructure at room temperature, Anal. Chem. 90 (16) (2018) 9821–9829, https://doi.org/10.1021/acs.analchem.8b01768.

[33] X. Ma, H. Zhang, C. Chen, Preparation and freshness detection of tofu based on In-doped CeO_2 ammonia gas sensor, Appl. Surf. Sci. 669 (2024) 160506, https://doi.org/10.1016/j.apsusc.2024.160506.

[34] S. Singh, K.Y. Shin, S. Moon, S.S. Kim, H.W. Kim, Phase-engineered $MoSe_2$/CeO_2 composites for room-temperature gas sensing with a drastic discrimination of NH_3 and TEA gases, ACS Sens. 9 (8) (2024) 3994–4006, https://doi.org/10.1021/acssensors.4c00793.

[35] C. Liu, H. Tai, P. Zhang, Z. Yuan, X. Du, G. Xie, Y. Jiang, A high-performance flexible gas sensor based on self-assembled PANI-CeO_2 nanocomposite thin film for trace-level NH_3 detection at room temperature, Sens. Actuators B Chem. 261 (2018) 587–597, https://doi.org/10.1016/j.snb.2017.12.022.

[36] N. Dogra, M. Singh, A. Kumar, S. Sharma, Selective room-temperature ammonia sensing using CeO_2-multiwalled carbon nanotube composite, Appl. Phys. A 129 (1) (2022) 24, https://doi.org/10.1007/s00339-022-06283-5.

[37] M.C. Naik, S.S. Potdar, S.V. Garg, G.M. Kharmate, K.S. Pakhare, Chemical combustion synthesis of CeO_2-ZnO nanocomposite and its application in ethanol sensing, J. Mater. Sci. Mater. Electron. 35 (32) (2024) 2045, https://doi.org/10.1007/s10854-024-13784-x.

[38] D. Xiong, M. Luo, Q. He, X. Huang, S. Cai, S. Li, Z. Jia, Z. Gao, Nb_2CT_x/$MoSe_2$ composites for a highly sensitive NH_3 gas sensor at room temperature, Talanta 286 (2025) 127446, https://doi.org/10.1016/j.talanta.2024.127446.

[39] L.-Y. Zhu, L.-X. Ou, L.-W. Mao, X.-Y. Wu, Y.-P. Liu, H.-L. Lu, Advances in noble metal-decorated metal oxide nanomaterials for chemiresistive gas sensors: Overview, Nano-Micro Lett. 15 (1) (2023) 89, https://doi.org/10.1007/s40820-023-01047-z.

[40] L. Zhang, C. Ma, J. Zhang, Y. Huang, H. Xu, H. Lu, K. Xu, F. Ma, Enhanced NO_2-sensing performances of CeO_2 nanoparticles on MoS_2 at room temperature, Appl. Surf. Sci. 600 (2022) 154157, https://doi.org/10.1016/j.apsusc.2022.154157.

Supporting information

CeO_2 and Nb_2CT_x heterojunction for efficient room-temperature NH_3 detection

Dingyuan Wang[a], Lizhai Zhang [a,b,c], Jiayuan Xu [d], Xinyu Lei [a], Henghui Sun [a], Fei Ma[b], Taotao Ai [a*], Paul K Chu [c*]*

[a] School of Materials Science and Engineering, Shaanxi University of Technology, Hanzhong 723001, Shaanxi, China

[b] State Key Laboratory for Mechanical Behavior of Materials, Xi'an Jiaotong University, Xi'an 710049, Shaanxi, China

[c] Department of Physics, Department of Materials Science and Engineering, and Department of Biomedical Engineering, City University of Hong Kong, Tat Chee Avenue, Kowloon, Hong Kong, China

[d] Natural Active Industrialization Engineering Technology Research Centre of Shaanxi Province, Shaanxi University of Technology, Hanzhong 723001, Shaanxi, China

*Address correspondence to: zhanglizhai0512@snut.edu.cn (L. Z. Zhang); aitaotao0116@126.com (T. T. Ai); paul.chu@cityu.edu.hk (P. K. Chu)

(1) The novelty of the current work.

Answer: The novelty of this paper is mainly reflected in the following two aspects: **(1) The oxygen vacancy (O_v) plays the important role in enhancing the NH_3 sensing response rather than BET surface area.** The BET surface areas of CeO_2 and Nb_2CT_x composites are measured in this paper. It's found that BET surface areas is larger as the Nb_2CT_x content is increased. While, the response of composites toward NH_3 is increased firstly and then decreased as the Nb_2CT_x content is increased, which is inconsistence with BET surface area results. According to the results of Raman and EPR measurement, the concentration of O_v is increased firstly and then decreased as the Nb_2CT_x content is increased, which is coincided with the results of NH_3-sensing response. Hence, the oxygen vacancy (O_v) plays the important role in enhancing the NH_3 sensing response rather than BET surface area. **(2) The effect of heterojunction on the NH_3-sensing response is studied.** According to the results of DFT calculation, without Nb_2CT_x, the bandgap of CeO2 is about 1.8 eV, behaving the poor conductivity. While, fabrication of CeO_2 and Nb_2CT_x heterojunction, the valence band and conduction band overlap at the interface giving rise to metallic properties. Electrons move from CeO_2 to Nb_2CT_x easily, leading to excellent NH_3 sensing response at RT. Introduction of O_v on the surface of CeO_2 could decrease the energy barrier at interface and thus promote the electron transfer at interface. In addition, based on the results of adsorption energy, the adsorption energy of CeO_2 and Nb_2CT_x heterojunction is much more negative than that of pure CeO_2 and Nb_2CT_x. Hence, Introduction of CeO_2

nanoparticles on the surface of Nb_2CT_x could improve the density of active sites for NH_3 adsorption and enhance NH_3-sensing response at RT.

(2) Although DFT calculations are presented, the theoretical explanations for enhanced sensing performance are not thoroughly connected to the experimental results. For example, the authors claim the synthesis of CeO_2 nanoparticles decorated on 2D Nb_2CT_x. However, in the DFT study, the analysis is based on separate layers of CeO_2 and Nb_2CT_x films, which does not accurately represent the synthesized composite structure.

Answer: In this paper, the theoretical calculation model of CeO_2 and Nb_2CT_x is different from actual structure. The DFT calculations is mainly used to elucidate the interfacial electronic states and adsorption ability of CeO_2/Nb_2CT_x heterojunction toward NH_3 molecular. The complex models may introduce more numerical instability factors, resulting in error accumulation or convergence problems. And thus, the accuracy and reliability of final results is decreased. In addition, the complex models may involve more parameters and settings, which may increase the unrepeatability of the experiment. Hence, a single-layer model was used to reveal the NH_3-sensing mechanism during the DFT calculations.

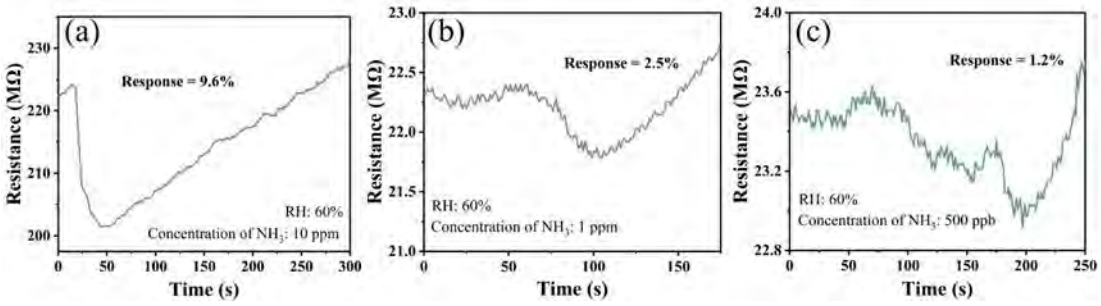

Fig. S1. Dynamic response-recovery curves of C/N-b for 10 ppm, 1ppm and 500 ppb NH_3 at RT.

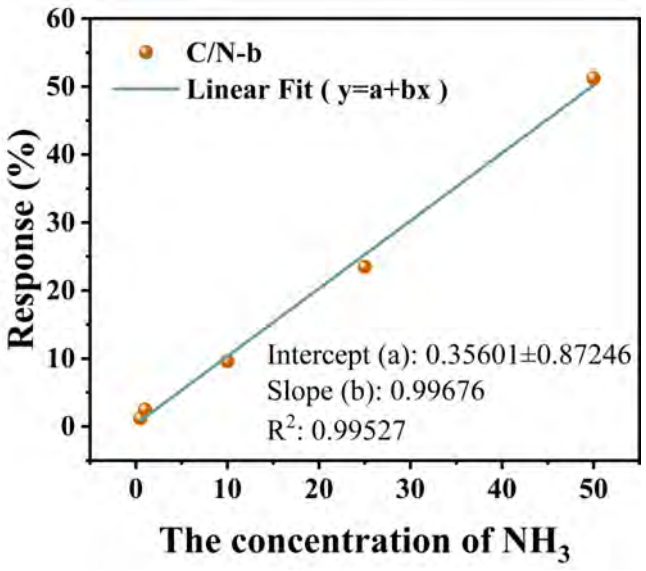

Fig. S2. The response of C/N-b toward 0.5 ppm, 1 ppm, 10 ppm, 25 ppm and 50 ppm NH_3 at RT. Fitting plot of C/N-b sensor.

The process of calculation of noise level (RMS_{Noise}) and limit of detection (LOD):

(1) Execute linear fit for the sensitivity curve versus NH_3 concentration of the sensor and then extract the slope value and standard error in the linear regime and the results were shown in Fig. S2.

(2) Take N = 50 data points at the baseline before NH_3 exposure and then plot the data (ΔR/R (%) versus Time (sec)) and then execute Polynomial fit (5th order).

(3) Take regular residual of polynomial fit and calculate the root-mean squared deviation (RMS_{Noise}) and LOD with Equation 1 and 2.

$$RMS_{Noise}\left(ppm^{-1}\right)=\sqrt{V_x^2/N} \quad \text{where} \quad V_x^2=\sum\left(Y_i-\bar{Y}\right)^2 \tag{1}$$

$$Limit\ of\ \text{detection}\left(ppm\right)=3\times\frac{RMS_{Noise}}{Slope} \tag{2}$$

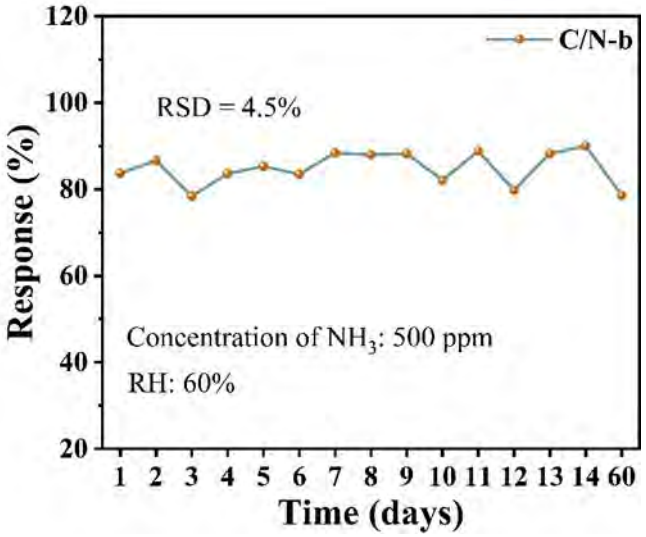

Fig. S3. Stability curve of C/N-b to 500 ppm NH_3.

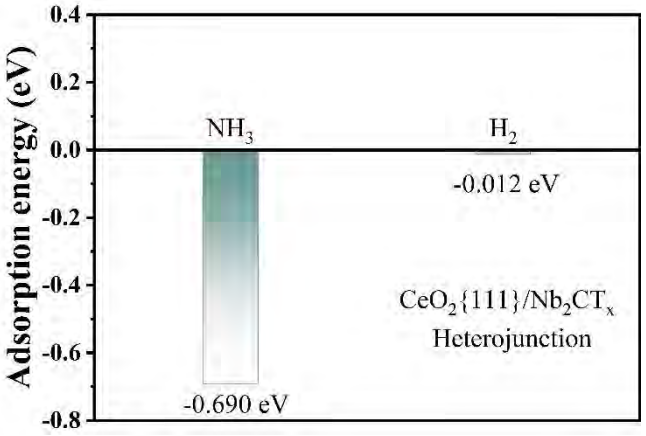

Fig. S4. Adsorption energies of NH_3 and H_2 on the surface of CeO_2.

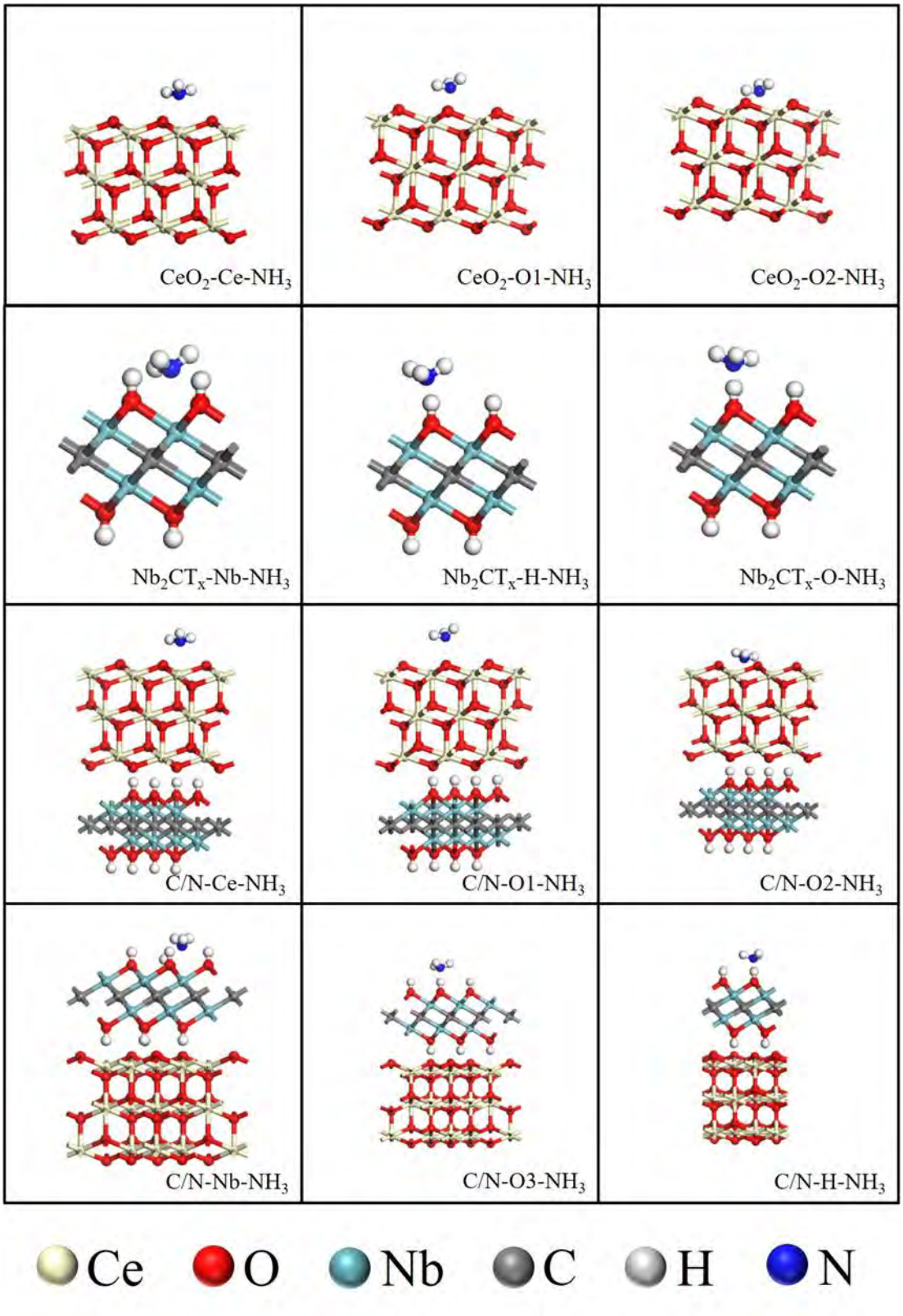

Fig. S5. Adsorption model diagram.

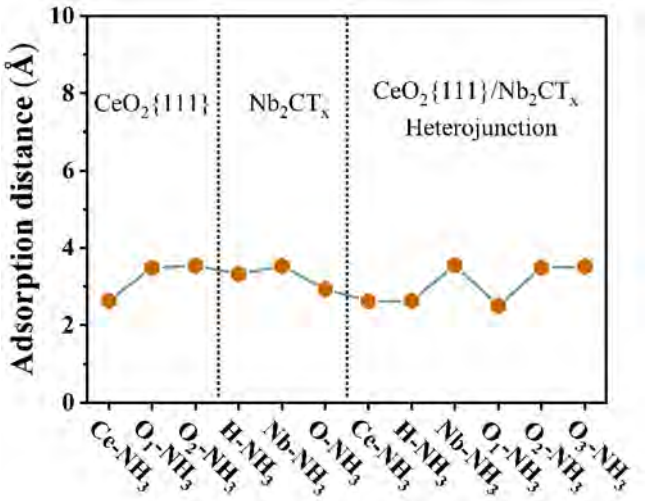

Fig. S6. The distance between adsorption sites and N atoms in NH_3.

Table S1. $I_D/I_{F_{2g}}$ value of C/N-a, C/N-b, C/N-c, and C/N-d.

	C/N-a	**C/N-b**	**C/N-c**	**C/N-d**
$\boldsymbol{I_D/I_{F_{2g}}}$	0.0451	0.0647	0.0383	0.0269

Table S2 Calculation of RMS noise and LOD for C/N-b composites sensors.

Sample	Slope (ppm^{-1})	RMS_{Noise}	LOD (ppm)
C/N-b	0.99676	0.00129	0.003882